Large-scale soil mapping using multi-configuration EMI and supervised image classification

C. Brogi[a], J. A. Huisman[a], S. Pätzold[b], C. von Hebel[a], L. Weihermüller[a], M. S. Kaufmann[a], J. van der Kruk[a], H. Vereecken[a].

[a] Agrosphere (IBG-3), Institute of Bio- and Geosciences, Forschungszentrum Jülich, Germany

[b] University of Bonn, Institute of Crop Science and Resource Conservation (INRES), Division Soil Science, Bonn, Germany

Corresponding author: Cosimo Brogi

c.brogi@fz-juelich.de

Abstract

Reliable and high-resolution subsurface characterization beyond the field scale is of great interest for precision agriculture and agro-ecological modelling because the shallow soil (~1-2 m depth) is responsible for the storage of moisture and nutrients that are accessible to crops. This can potentially be achieved with a combination of direct sampling and Electromagnetic Induction (EMI) measurements, which have shown great potential for soil characterization due to their non-invasive nature and high mobility. However, only a few studies have used EMI beyond the field scale because of the challenges associated with a consistent interpretation of EMI data from multiple fields and acquisition days. In this study, we performed a detailed EMI survey of an area of 1 km^2 divided in 51 agricultural fields where previous studies showed a clear connection between crop performance and soil properties. In total, nine apparent electrical conductivity (ECa) values were measured at each location with a depth of investigation ranging between 0-0.2 to 0-2.7 m. Based on the combination of ECa maps and available soil maps, an a priori interpretation was performed and four sub-areas with characteristic sediments and ECa were identified. Then, a supervised classification methodology was used to divide the ECa maps into areas with similar soil properties. In a next step, soil profile descriptions to a depth of 2 m were obtained at 100 sampling locations and 552 samples were analyzed for textural characteristics. The combination of the classified map and ground truth data resulted in a 1 m resolution soil map with eighteen units with a typical soil profile and texture information. It was found that the soil profile descriptions and texture of the EMI-based soil classes were significantly different when compared using a two-tailed *t*-test. Moreover, the high-resolution soil map corresponded well with patterns in crop health obtained from satellite imagery. It was concluded that this novel EMI data processing approach provides a reliable and cost-effective tool to obtain high-resolution soil maps to support precision agriculture and agro-ecological modelling.

1. Introduction

The demand for reliable high-resolution soil maps at scales larger than the field-scale is of great interest for precision agriculture and agro-ecological modelling because local differences in shallow soil properties (~1-2 m max depth) are known to influence soil water movement and retention, nutrient availability, and root growth. Various thematic maps may provide information on soil characteristics (e.g., geological, soil, and yield potential maps). However, these available maps typically do not have the required resolution to support the identification and management of within-field differences in crop performance (Franzen et al., 2002; Nawar et al., 2017), because they are based on sparse and time consuming direct soil sampling.

Hydrogeophysical methods provide a viable alternative to point-scale direct sampling (Robinson et al., 2008). In particular, electromagnetic induction (EMI) measurements have shown promise to characterize spatial variability in soil properties because of its high mobility (Robinson et al., 2012; van Dam, 2012). EMI measures the apparent electrical conductivity (ECa) of the ground, which can be related to soil water content, pore water conductivity, soil porosity, and soil texture (Corwin and Lesch, 2003; Sheets and Hendrickx, 1995).

At the field-scale (~1-10 ha) and beyond, a range of studies successfully used EMI for mapping relevant soil properties, such as the variation in soil texture and layering (Cockx et al., 2007; Kelley et al., 2017; Mertens et al., 2008), soil salinity (Huang et al., 2017a; Yao et al., 2016), soil water dynamics (Huang et al., 2017b), organic matter (Huang et al., 2017c), and CEC (Machado et al., 2015). In addition, EMI has been used to quantitatively link ECa, soil characteristics, and crop performance during periods of water stress (Rudolph et al., 2015). Despite these promising results, the vertical resolution of soil characteristics obtained from EMI measurements was low in most studies. Recently, new EMI instruments with multiple coil separations and orientations have been introduced that provide improved vertical resolution, but they have not been widely used for soil characterization yet (von Hebel et al., 2014).

EMI measurements are also used for soil characterization at scales larger than the field-scale (> 10 ha) (e.g., Ding and Yu, 2014; Frederiksen et al., 2017; Zare et al., 2016). So far, EMI measurements were performed in a limited time-window in such large-scale studies, thus minimizing temporal variations in dynamic soil characteristics within the EMI survey (e.g. water content and soil temperature) (Frederiksen et al., 2017). However, this may not be feasible in complex agricultural areas where multiple fields are managed with different crops with variable harvest times. In such cases, it is expected that the spatial variation in ECa is difficult to interpret in terms of a single soil property.

In the absence of direct correlations between EMI measurements and a single soil property, a range of studies have used clustering or classification of EMI data to identify zones with similar properties. For example, clustering of ECa maps has been widely used to identify management zones that can be treated homogeneously within precision agricultural applications. Most of such studies relied on a combination of EMI measurements, direct soil sampling, and yield maps (e.g., Galambošová et al., 2014; King et al., 2005; Oldoni and Bassoi, 2016; Taylor et al., 2003; Uribeetxebarria et al., 2018). Some studies also considered other proximal and remote sensing techniques in addition to EMI to identify management zones such as ground penetrating radar, gamma-ray spectrometry, and hyperspectral airborne and satellite images (Castrignano et al., 2012; Ciampalini et al., 2015; De Benedetto et al., 2013; Huang et al., 2014; Jing et al., 2017;

Triantafilis et al., 2009). However, the majority of studies dealing with clustering of EMI data was focused on the field-scale and used only a single or limited number of EMI configurations. The applicability and utility of clustering EMI data to identify areas with similar soil properties have not been demonstrated yet for large-scale multi-configuration EMI data sets consisting of EMI measurements taken at different times and for a range of investigation depths.

In this study, we focus on an agricultural area of 1.0 km^2 near Selhausen (North-Rhine Westphalia, Germany) characterized by complex patterns in soil properties that are known to affect crop performance. These observed patterns in crop performance are not captured in detail by available soil maps. Therefore, the objective of this study is to obtain a high-resolution soil map with a detailed and quantitative representation of horizontal and vertical variability of soil properties from an extensive multi-configuration EMI survey that was carried out throughout the year 2016. For this, a supervised classification methodology adapted from remote sensing will be used to identify areas with similar soil properties from multi-configuration EMI data, and a limited number of ground-truth points will be used to obtain soil profile and texture information for each of these areas. Statistical analysis will be used to evaluate whether soil properties are significantly different between these areas. In a final step, the ability of the high-resolution soil map to capture patterns in plant stress will be evaluated using a comparison with crop performance patterns obtained from satellite images.

2. Materials and methods

2.1 Study area

The study was conducted in an agricultural area near Selhausen (Germany). It is located in the Rur Catchment (North-Rhine Westphalia) approximately 40 km west from Cologne (50°51’56”N 6°27’03”E). The shape of the study area is a square of 1x1 km bearing 12.75° east (Figure 1). The climate is characterized by an average precipitation of 715 mm and a mean annual temperature of 10.2°C (Rudolph et al., 2015). The altitude ranges between approximately 101 m and 113 m a.s.l.

The shallow geology consists of quaternary sediments divided in two main geological areas: the upper terrace and the lower terrace. According to the 1:5,000 soil map of this area (Figure 1b), the upper terrace in the eastern part consists of Pleistocene sand and gravel sediments associated with the Rhine/Meuse river system (Röhrig, 1996). It is characterized by a system of subsurface channels filled and buried by aeolian sediments of variable thickness (Klostermann, 1992; Patzold et al., 2008; Vandenberghe and Van Overmeeren, 1999). The lower terrace in the western part consists of Pleistocene loess sediments and translocated loess sediments from the Holocene (Figure 1b). Similar to the upper terrace, part of the translocated loess of the lower terrace is deposited on Pleistocene/Holocene sand and gravel sediments (Röhrig, 1996). The two terraces are separated by a slope that ranges from 2% to 10% with a westbound dip and an approximately NNW-SSE strike.

The dominant reference soil groups in the area are Cambisols, Luvisols, Planosols, and Stagnosols (WRB, 2015). The area is divided into 51 fields ranging in size from 0.5 to 10.0 ha. The fields are cultivated in rotation with winter wheat, barley and sugar beet. Occasionally potato, maize, oilseed rape, and oats are grown. According to the German cadaster, there are 52 different land owners but the effective number of farmers is lower than twenty because of kinship and lease. The large number of active farmers leads to a heterogeneous field management.

Previous studies highlighted the influence of subsurface heterogeneity on crop performance in several fields located on the upper terrace (Rudolph et al., 2015; Simmer et al., 2015; Stadler et al., 2015). This is illustrated in a satellite image from a drought period (Figure 1a) where patterns in crop performance are visible in the upper terrace (fields F14a, F17a, F22b, F23, F24a-b, F47, and F49 in Figure 1a). Similar patterns are visible in the lower terrace, but these have not been studied yet (fields F39 and F40 in Figure 1a).

Figure 1c presents the soil taxation map (NRW, 1960) of the study area (sheets 510410 (west) and 510411 (east)). This map shows the yield potential of the agricultural land at the scale of 1:5,000 and provides soil profile information up to a depth of 1.0 meter. In general, this map is more detailed than the 1:5,000 soil map and represents the most detailed available soil information for the selected study area. However, it is not capable of representing the complexity of the subsurface for this particular study area. This is evident from a comparison with the observed patterns in crop performance shown in Figure 1a. The lack of detail in the soil taxation map is mainly due to the low sampling density of one drilling per 40-50 m used during mapping.

2.2 Electromagnetic Induction (EMI) measurements

Frequency domain EMI systems generate a fixed frequency alternating current through a transmitter coil, which generates the primary magnetic field. This primary magnetic field induces eddy currents in the electrically conductive subsurface, which in turn generate a secondary magnetic field. The ratio between the secondary and primary magnetic field is related to the apparent electrical conductivity (ECa) and, to a lesser degree, to the apparent magnetic permeability over a certain depth range that depends on the source-receiver coil distance and orientation (Keller and Frischknecht, 1966; Ward and Hohmann, 1988).

2.2.1 EMI instrumentation

In this study, we simultaneously used the CMD-MiniExplorer (ME) with three receiver coils and coil separations of 32, 71, and 118 cm oriented in vertical coplanar configuration (VCP) and a custom-made CMD-MiniExplorer - Special Edition (SE) with six receiver coils and coil separations of 35, 50, 71, 97, 135, and 180 cm (GF instruments, Brno, Czech Republic) oriented in horizontal coplanar configuration (HCP) to collect data using both VCP and HCP configurations at the same time (Table 1).

Figure 2 shows the depth-specific sensitivity of all EMI measurements in VCP and HCP orientation to the subsurface electrical conductivity distribution (McNeill, 1980). The VCP orientation is most sensitive to the shallow subsurface and becomes less sensitive with increasing depth, while the HCP orientation is less sensitive to the shallow subsurface and the sensitivity peaks at a depth of around 0.4 times the coil separation (McNeill, 1980). As a rule of thumb, the depth of investigation (DOI) for VCP is approximately 0.75 times the coil separation (s) and the DOI for HCP is approximately 1.5 times the coil separation. This result in DOI's ranging from 0-24 to 0-270 cm for our measurements set-up.

2.2.2 EMI survey

The EMI measurements on the 51 agricultural fields (102 ha) shown in Figure 1a were performed between April and December 2016 within a few days after harvest of the different crops. For each field, a standardized measurement protocol based on best practice EMI measurements was followed (European Committee for Standardization, 2011). The EMI instruments were mounted on two plastic sleds that were separated by 1.5 m. A quad-bike was used to pull the sleds while keeping a distance of 4 m from the first sled. The driving speed ranged from 5 to 7km/h. The sampling frequency was 5 Hz, which resulted in an in-line resolution of approximately 0.3 m with a track spacing of 2.0 to 2.5 m. The EMI measurements were made in the direction of ploughing to avoid possible effects of terrain roughness on the EMI measurements.

A single frequency GPS (NovAtel inc., Calgary, Canada (see Rudolph et al., 2018)) was used to provide spatial position during the measurements from April to October 2016 (a total of 76 ha). A TRX centerpoint DGPS system (Trimble inc., Sunnyvale, USA) with higher accuracy was used from November to December 2016 for a total of 21 ha. Despite the difference in accuracy between the single frequency GPS system (meter accuracy) and a DGPS system (cm accuracy), we considered the measurements obtained with the two GPS systems as equally reliable for the purpose of this study. Each field was measured continuously and the first line of EMI measurements was repeated at the end of each field survey to verify that no unexpected shifts in the measured ECa occurred. In general, the difference in ECa values measured at the start and at the end of each survey was negligible.

2.2.3 Data filtering and interpolation

The CMD-MiniExplorer and the CMD-MiniExplorer Special Edition have been factory-calibrated using the supplied handle (i.e., a crutch). Therefore, it is not necessary to perform in-field zeroing. Both devices also internally compensate for temperature changes during a survey with a stability of 0.1 mS/m per °C (GF_Instruments, 2011). Nevertheless, negative ECa values were measured in this study as already observed in previous studies (Rudolph et al., 2015; von Hebel et al., 2014). Some studies have therefore calibrated the ECa measurements with independent electrical resistivity tomography (ERT) data (Lavoué et al., 2010; Shanahan et al., 2015) in order to obtain quantitative EMI data that allow inversion (Mester et al., 2011; von Hebel et al., 2014). Alternatively, calibration can be achieved using a metal sphere or by measuring at multiple elevations (Tan et al., 2018; Thiesson et al., 2014). Since repeated calibration is difficult to achieve for the EMI survey presented here, we applied a correction based on a linear regression between EMI measurements made with the sled and the supplied handle for each EMI coil configuration. In this approach, it is assumed that the required calibration of each EMI coil configuration is relatively stable in time, which is consistent with our experience with EMI calibration.

Since measured ECa values are rarely normally distributed (Minsley et al., 2012), we applied an histogram-filtering technique following von Hebel et al. (2014) to identify and exclude outliers. The filter divides the data into 15 bins. Bins containing <0.5% of the data were removed. Afterwards, neighboring ECa measurements that showed differences larger than 1 mS/m were removed to avoid unrealistically high lateral ECa variation. In a next step, the filtered data of each coil configuration were interpolated to a regular 1 by 1 m grid using ordinary Kriging with an exponential semivariogram. The individual interpolated surfaces for each coil configuration were merged together in a raster mosaic dataset.

2.2.4 Temperature correction

To standardize the EMI data to a reference temperature of 25°C, we performed a correction for soil temperature using the approach of Campbell et al. (1949).

$$EC_a^{25} = f_T EC_a^T, \tag{1}$$

where ECa^T is the ECa measured at soil temperature T and f_T is a temperature correction factor given by

$$f_T = 0.4470 + 1.4034e^{-T/26.815} \tag{2}$$

as proposed by Sheets and Hendrickx (1995), corrected by Corwin and Lesch (2005) and used in many time lapse EMI studies (e.g. Robinet et al., 2018). The average soil temperature between 8 AM and 8 PM at all measurement days was obtained by averaging the measurements from three soil temperature sensors installed in field F10 at a depth of 0.5 m. The minimum soil temperature was measured on the 5th of December (4.7°C when field F50 was measured), while the highest temperature was measured on 15th of September (20.8°C when fields F38 and F39 were measured). It is important to realize that this temperature correction will not be able to overcome all differences in mean ECa between fields, since EMI data were acquired in different seasons and after different agricultural management (e.g., type of crop, timing of fertilization).

2.3 Classification of ECa maps

A flowchart of the classification methodology including aspects of preprocessing as well as the selection of sampling locations for ground truth data is shown in Figure 3. The following analyses were performed using ArcGIS Desktop software. The first step of the classification was to merge the EMI measurements obtained with the six coil separations in the HCP orientation. For this, we used a raster processing composite band tool (ESRI, 2017) to generate a multiband raster dataset, where HCP coils with increasing separation represent the different bands (Figure **4**). We decided not to add the VCP configurations to the multiband image because the stronger sensitivity to shallow layers resulted in higher noise and because the relatively homogeneous ploughing horizon of ~30 cm thickness resulted in relatively constant ECa values within each single field for these configurations. However, the EMI measurements in VCP mode will be used in the following to support the interpretation of the EMI data.

To classify the multiband raster data, a supervised classification method was used. In a first step, the number of soil classes and their interpretation need to be defined. For this interpretation, information contained in the nine ECa maps, the soil map, the soil taxation map, as well as expert knowledge from previous studies and field observations were taken into account. As a result of this interpretation process, the amount and type of soil classes is known for each field.

In a next step, the multiband raster of EMI data was used to classify the survey area field-by-field. This was necessary because EMI data were found to vary between fields due to other factors besides soil properties (see results section for a more detailed analysis of this variability). For each field, areas belonging to a specific soil class were identified within the multiband raster data (so-called training areas). This was achieved by visualizing different combinations of EMI coil separations displayed with RGB composite colors (see Figure **4** for one possible example). After the training areas were selected for each soil class, histograms of ECa values for each class and band as well as scatter plots of ECa values for all classes for different combinations of bands were used to evaluate the distribution and separation of the classes in the six-dimensional space of the measured ECa values. When it was not possible to achieve a proper separation of the clusters in all fields using the given number and interpretation of classes, then the interpretation was reviewed and the process was repeated until a proper cluster separation was achieved on all fields.

After defining the training areas for a given field, a Maximum Likelihood classification (ESRI, 2017) was used to classify all raster cells of a field. For this, the mean and the covariance matrix of the training areas were calculated (Ball and Hall, 1965; ESRI, 2014; Richards, 1999). Based on this, the statistical probability that a particular cell belongs to each class was calculated and the cell was assigned to the class with the highest probability. After this classification, a raster map of the field is obtained where every cell is assigned to the most probable class.

After the classification of each field, the results were merged together to obtain one classified map of the whole study area. Next, two filtering procedures were applied to remove small areas characterized by a single or few cells as well as to smooth the boundaries between different classes. First, a majority filter (ESRI, 2017) was used to replace cell values based on the value that occurs most often within the eight neighboring cells. This replacement occurred only when the number of neighboring cells from the same soil class is large enough to be the majority (e.g. 5 out of 8 cells) (ESRI, 2014). Second, a boundary clean filter (ESRI, 2017) relying on an expand-and-shrink method in order to clean the boundaries from ragged edges between different soil classes was used. A sorting based on the size of different zones represented by a single class was applied to facilitate the expansion of large zones over small ones (ESRI, 2014).

2.4 Soil sampling for ground truth information

Based on the final map obtained from the classification of EMI data, 100 soil augering locations were selected where soil profile descriptions and soil samples were acquired. The sampling points were distributed amongst all the soil classes and the number of points per soil class was based on the total area of the soil class itself with a minimum of three sampling locations per soil class. For each of the 100 points, a random location within the assigned class was determined. Each location was at least 2.5 m away from the boundary between two soil classes. Also, locations within the same soil class were separated by at least 150 m. In January and February 2017, all locations were visited using a DGPS system (Trimble inc., Sunnyvale, USA) and a Pürckhauer auger was used to sample and describe the soil up to a maximum depth of 2.0 m.

The maximum augering depth at each location varied considerably because of the presence of horizons with high gravel content or strong cementation. For each sampling location, a soil profile description was obtained with information on horizon type, horizon thickness, total depth, and color. To delineate horizons in the field, texture was estimated by feel (“hand texturing”) (Sponagel et al., 2005; Vos et al., 2016). For each horizon, at least one soil sample was collected. When layers with different texture were identified in a single horizon, multiple samples were collected. All soil samples were stored in a refrigerated room until the gravimetric water content was estimated by drying the sample at a temperature of 105°C for 36 hours. The weight fraction of gravel (> 2 mm) was determined using sieving. Afterwards, the texture of each sample was analyzed with a combined sieving and pipette method using a Sedimat 4-12 apparatus (UGT, Umwelt Geräte Technik GmbH, Münchenberg, Germany).

The soil profiles of all ground truth locations within a single soil class were averaged to obtain a typical soil profile with information on horizon type, depth, texture, and gravimetric water content for that particular class. To compare different soil classes, the soil classes were ordered according to decreasing average ECa. Two tailed *t*-tests were performed between matching horizons of two adjacent soil classes to establish whether there are statistically significant differences. For this statistical analysis, the horizons Ap and AB were considered as a single horizon. The null-hypothesis of equal means in the *t*-test was rejected when the computed *t*-value was higher than the 5 % level of significance (2.5 % in each tail).

2.5 Comparison with satellite image

To test the potential of the EMI-based soil map to identify areas with variable crop growth, we compared it with observed field-scale patterns in crop growth derived from remote sensing. For this, we used a WorldView-2 panchromatic satellite image with 0.5 m resolution provided by DigitalGlobe within ArcGIS Basemap (ESRI, 2016). The image was collected during a drought period in July 2015 (Figure 1a). Here, we analyze a set of fields that were cropped with sugar beet in 2015 (F05,F07, F08, F17a, F22b, F23, F24, F39, F40 and F49) since sugar beet is known to show visual signs of drought stress in this area (Rudolph et al., 2015). In each of the sugar beet fields, areas with relatively stressed crops (light green) and areas with relatively healthy crops (dark green) were manually digitized on the satellite image.

In order to quantify the correspondence between each class of the soil map and the crop performance derived from the satellite image, the number of cells located on stressed and healthy crops was determined for each class of the soil map for each field. If more than 50% of the cells of a soil class for a particular field were stressed crops, the soil class was assumed to correspond with stressed conditions (and vice versa). The correspondence of each soil class with the satellite image was quantified using the true positive ratio (TPR), which is the fraction of cells correctly classified as being stressed, and the true negative ratio (TNR), which is the fraction of cells correctly classified as healthy crops. Due to these definitions, TPR and TNR can range from 50 to 100%.

3. Results and discussion

3.1 Large-scale EMI survey

The ECa maps presented in Figure 5 show that the study area can be divided in four sub-areas (Figure 5c), each with characteristic sediments and ECa values and patterns. This subdivision was performed by comparing the patterns in ECa maps (Figure 5a-f) and their general ECa values (Table 2) with the geometry of the soil map (Figure 5a) and, to a lesser degree, of the soil taxation map (Figure 5b). Here, it is assumed that the soil maps provide reliable information on the type and origin of the sediments, albeit with a low resolution because of the lower density of the ground truth information used to create the maps. Therefore, the joint interpretation of ECa maps (horizontal geometry) and soil maps (type and origin of sediments) results in a more reliable subdivision of the study area. From east to west, the following sub-areas were identified: a buried paleochannel system on the upper terrace (sub-area A in Figure 5c), a transition zone associated with a slope heading N-S (sub-area B in Figure 5c), a relatively homogeneous area in the center (sub-area C in Figure 5c), and a second heterogeneous area in the west (sub-area D in Figure 5c). In the following, the ECa maps from these four sub-areas are discussed in more detail.

Sub-area A was partly studied by Rudolph et al. (2015), and is characterized by relatively low ECa values compared to the rest of the study area (Table 2). The geometry of this sub-area agrees well with the Pleistocene loess deposits on sand and gravel described in the soil map (Figure 1b). Therefore, it is assumed that the entire sub-area A is characterized by paleochannels cut in sandy-gravel material and then filled by finer loess sediments. These paleochannels are characterized by a relatively higher ECa because of the larger thickness of the loess sediments with higher silt and clay content and higher water storage capacity (Rudolph et al., 2015). The average ECa generally increased with DOI for both VCP and HCP coil configurations (Table 2). However, the range of ECa values is relatively small, especially when compared to the rest of the study area. A geomorphological interpretation of the pattern of buried channels indicates that the stream type was an anastomosing fluvial system with multiple channels (Rosgen, 1994).

The transition zone represented by sub-area B coincides with the slope that strikes N-S across the study area. The morphology of the area, the soil map description (Pleistocene loess sediments), and the patterns in the ECa maps suggest the presence of Holocene slope deposits located on Pleistocene loess sediments. Some of these deposits are partly anthropogenic since the slope has been repeatedly flattened to facilitate agricultural management. A more detailed description of the geomorphology of this sub-area is provided in Appendix A. In general, the ECa values increase with DOI for both VCP and HCP configurations and they are higher compared to sub-area A (Table 2). The increase of ECa with DOI is most pronounced for the deeper sensing configurations (HCP with 130 cm and 180 cm coil separation). This is probably related to the presence of fine sediments in the deeper layers compared to the shallow surface.

The ECa values in sub-area C also showed a general increase with DOI and were relatively higher when compared to the other three sub-areas (Table 2). This area was previously described as a homogeneous lower terrace using measurements in VCP and HCP configuration with a small offset (Rudolph et al., 2015). The soil taxation map (Figure 1c) describes this area as relatively homogeneous with loamy sediments, while the soil map (Figure 1b) indicates Pleistocene loess and translocated loess. The higher ECa values in sub-area C suggest the presence of soils and sediments with higher clay content. The remains of irrigation channels and water ponds are visible in the ECa maps of this sub-area (Figure 5d), and these features are described in detail in Appendix A.

The heterogeneous sub-area D was measured for the first time with EMI in this study. Generally, the average ECa values again increased with DOI both for the VCP and for the HCP coil configurations. The pattern visible in the ECa map (Figure 5) suggests that the subsurface of sub-area D is also characterized by a buried fluvial system and that the paleochannels are again characterized by a relatively higher ECa.. However, the different geometry of the buried channels and the higher ECa values suggest a different type of fluvial activity. This is corroborated by the soil map that indicates translocated loess sediments on sand and gravels (Holocene-Pleistocene). Furthermore, the buried channels are straighter and wider compared to sub-area A. Likely, the depositional environment was closer to a braided fluvial system (Rosgen, 1994).

3.2 Heterogeneity at the field-scale

Besides the large-scale patterns in ECa values, field-scale variability in ECa values is also apparent. For example, fields F08 and field F24a-b were managed differently before the EMI data acquisition that took place on the same day (

Figure **6**a). Field F08 and field F24a were cropped with wheat by two different farmers, while field F24b was cropped with barley. Therefore, it is assumed that the observed differences in ECa for field F08 and field F24a-b are related to the different management that has resulted in different soil water content or different pore water conductivity at the time of data acquisition. Similarly,

Figure **6**b shows variations in ECa values between adjacent fields that were not measured at the same time. As in the previous case, part of the observed variation is related to differences in field management. More importantly, there are differences due to the variable amount of precipitation in the days before data acquisition, which obviously affects soil water content and thus ECa values.

Although these two examples illustrate that variable management and timing of EMI data acquisition affected the ECa maps, it can be seen that the characteristics of the subsurface in terms of layering and texture are still identifiable, since a range of features that cross the field boundaries are apparent (

Figure **6**b). Here, it is important to emphasize that the adopted approach for ECa correction (calibration and temperature) was not expected to correct these differences in ECa between fields, since they are likely related to variations in soil water content and pore water conductivity. To overcome this secondary variability in ECa as much as possible, it was required to apply the classification methodology to each field independently.

3.3 Definition of the classes

After subdividing the study area in four different sub-areas, it was assumed that the soils in each sub-area are different because of the different type and age of the sediments. Further subdivision within each sub-area was performed prior to the classification of each field.
In sub-area A, the best distribution and separation of the clusters in the six-dimensional space provided by the EMI data in the multiband raster was achieved by using four soil classes, which are named A1a, A1b, A1c, and A1d in the following. These soil classes showed a general decrease in ECa from class A1a to A1d (Table 3).

In sub-area B, an appropriate separation of clusters was obtained using a total of five soil classes divided in two groups: two soil classes representing natural soils (B1a and B1b) and three representing anthropogenic soils (B2a, B2b, and B2c). Generally, ECa was higher in natural soils compared to anthropogenic soils (Table 4). Moreover, ECa decreased from soil class B1a to B1b and from soil class B2a to B2c (Table 4).

In sub-area C, a clear subdivision can be made between anthropogenic soils (Figure 5d) and the surrounding natural soils. The anthropogenic soils were divided in buried irrigation channels (class C2a) and buried water ponds (class C2b, Table 5). These soil classes were manually determined in the multiband raster because of their evident geometry (Figure 5d and Appendix A) and subsequently removed from the multiband image to avoid any influence in the classification process. The remaining area of sub-area C is apparently homogeneous according to the 1:5000 soil map and the soil taxation map (Figure 1b-c). However, the range of ECa (e.g., from 9.2 to 35.1 mS/m in HCP 35 cm and from 13.8 to 34.2 mS/m in HCP 180 cm) suggested further subdivision and the use of two soil classes C1a and C1b with different ECa (Table 5).

In sub-area D, the best distribution and separation of clusters was provided by using five soil classes. The four soil classes D1a, D1b, D1c, and D1d represent natural soils, and soil class D2a represents an anthropogenic structure in field F39. The ECa of soil class D2a was highest, then the ECa decreased from soil class D1a to D1d (Table 6).

Using these classes, the multiband ECa image of each field was classified. This resulted in a high resolution soil map composed of four sub-areas divided in a total of 18 soil classes. In the following, the results for each sub-area are presented separately to facilitate the description and the understanding of the high resolution soil map obtained by combining the classification results with the ground truth sampling.

3.4.1 Classified ECa map of sub-area A

The results of the supervised classification of sub-area A are shown in

Figure 7b while the average soil profiles of each soil class are shown in

Figure 7c. The soil profiles of each soil class are richer in fine sediments (clay and silt) in the Ap-AB, and Bw horizons characterized by Aeolian sediments. The deeper horizons consisted of coarser sediments composed of Pleistocene sand and gravels. The average ECa for each configuration decreased from soil class A1a to class A1d (Table 3). This may be due to the decreasing maximum depth of the Bw horizon that consists of finer sediments (

Figure 7c). A pairwise *t*-test between neighboring soil classes indicated that this maximum depth was significantly different only between classes A1a and A1b ($p = 0.040$). However, the textural data showed a significant difference ($p = 0.031$) in gravel content between the Ap-AB horizon of soil class A1b (16.7 %) and A1c (29.8 %). In addition, the clay content of the AP-AB horizon in class A1c (14.4 %) was significantly higher ($p = 0.034$) than that of class A1d (12.9 %).These textural characteristics are in agreement with the decreasing average ECa from soil class A1b to A1d. The average texture of all soil profiles for sub-area A-D and the results of all pairwise *t*-tests within each sub-area are provided in the supplementary information.

3.4.2 Classified ECa map of sub-area B

The results of the supervised classification of sub-area B are shown in Figure 8b and the average soil profiles are shown in Figure 8c-d. Compared to sub-area A, the soil profiles in this sub-area generally have a Bg horizon below the Bw horizon. Moreover, the 2C horizon consisting of coarse sediments that is common in sub-area A was found only in one of the five soil classes of sub-area B. An Ap-AB horizon was always found on top of each profile.

Table 4 shows that the average ECa is higher in soil class B1a compared to B1b. Together with the presence of the 2C horizon in soil class B1b, this suggests that B1b represents areas in which the 2C horizon, typical of sub-area A, is present below slope deposits. Although there were no significant differences in horizon depth between class B1a and B1b, we did observe significant differences in texture as indicated in Figure 8c. The most evident was the higher clay content of the Ap-AB, Bw, and Bg horizons of class B1a (15.9 %, 17.3 %, and 22.5 % compared to 12.3 %, 16.4 % and 18.1 % with $p = 0.005$, $p = 0.006$, and $p = 0.002$). In addition, the sand content of the Ap-AB and Bg horizons of class B1a was lower than in B1b (15.1%, and 12.8 % compared to 19.2 %, and 17.8 % with $p = 0.002$, and $p = 0.012$). Again, these textural differences are consistent with observed differences in ECa. In contrast with the decrease in average ECa, the gravel content of the Bg horizon of soil class B1a was significantly higher than that of class B1b (12.8 % compared to 1.6 %, $p = 0.014$). However, we assume that this difference in gravel content is secondary given the aforementioned differences in textural characteristics and layering of these two classes.

Soil classes B2a, B2b, and B2c are characterized by anthropogenic deposits in the first ~70-95 cm of the profile. The profiles of classes B2a and B2b are relatively similar, and no significant differences were found in horizon depth. Again, the texture showed meaningful differences. The clay content of the Ap-AB horizon of class B2a was significantly higher than that of B2b (15.1 % compared to 12.0 %, $p = 0.002$). Even though the anthropogenic horizon of soil class B2b showed a significantly higher sand content (19.7 % compared to 15.1 %, $p = 0.020$), the profile and texture were considered to be consistent with the higher average ECa of class B2a. The profile of soil class B2c is the only one without a Bg horizon. At the same time, the Ap-AB horizon of this class is characterized by a significantly higher gravel content compared to class B2b (24.3 % in class B2c compared to 3.5 %, $p = 0.001$). Furthermore, the sand content of the Ap-AB horizon is significantly higher in soil class B2c (21.7 % compared to 17.1 %, $p = 0.010$). This is in agreement with the lower average ECa in class B2c compared to class B2b and apparently compensates the significantly higher clay content of horizon Ap-AB of class B2c (14.9 % in class B2c compared to 12.0 % in class B2b, $p = 0.006$). Note that each of these anthropogenic soil classes was characterized using only three ground truth sampling locations, so that the provided interpretation should be considered with some caution.

3.4.3 Classified ECa map of sub-area C

The results of the supervised classification of sub-area C are shown in

Figure 9b and the average profiles of the four soil classes are shown in

Figure 9c-d. The profiles in this sub-area are relatively simple. A Bg horizon is consistently present below a Bw horizon and an Ap-AB horizon is always found on top of each profile.

The two soil classes associated with natural deposits (C1a and C1b) did not show significant differences in the horizon depths, and also no significant differences in texture were found. This could be expected considering the subtle differences in ECa between the two classes (Table 5). However, a significant difference in gravimetric water content was found for the Bg horizons. The gravimetric water content was significantly higher in soil class C1a (16.0 % compared to 14.1 %, $p = 0.021$), which is in agreement with the higher average ECa for this class, and this may be related to differences in bulk density at depths. Nevertheless, these two classes are considered to be similar and could be merged according to the ground truth information.

For the anthropogenic soil classes (C2a and C2b), the soil profiles differ in the thickness and thus the maximum depth of the anthropogenic horizon and the depth of the Bg horizon. The anthropogenic horizon extends to 112.5 cm in C2b compared to a mean depth of 51.0 cm in C2a ($p = 0.036$). In addition, the top of the Bg horizon is 129.0 cm in C2b compared to 86.0 cm in C2a ($p = 0.034$). This is in agreement with the interpretation of anthropogenic fillings of old irrigation networks (class C2a) and water ponds (class C2b) that are further discussed in Appendix A.

3.4.4 Classified ECa map of sub-area D

The results of the supervised classification of sub-area D are shown in Figure 10b, while the average profiles of each soil class are shown in Figure 10c and Table 6 provides the average ECa values and the standard deviation for each of the four soil classes. The soil profile of each soil class is characterized by finer sediments in the top horizons (Ap-AB, Bw, and Bg) above a coarser 2C horizon. Another anthropogenic soil class with an Ap-AB horizon over an anthropogenic layer is also present in this sub-area.

The four soil classes D1a-d showed similar horizon types. An Ap-AB horizon was found over Bw and Bg horizons with variable thickness followed by a coarser 2C horizon. Similar to sub-area A, the decrease in depth to the coarse 2C horizon corresponds with a decrease in average ECa going from class D1a to class D1d (Table 6). The difference in depth to the 2C horizon are statistically significant between classes D1b and D1c (122.7 cm in class D1b and 83.3 cm in class D1c, $p = 0.034$). This difference was not statistically different between classes D1a and D1b, but the textural analysis revealed a significant difference in gravel content of the Ap-AB horizon (higher in class D1b with 4.3 % compared to 0.9 %, $p = 0.044$) and in sand content of the Bw horizon (again higher in class D1b with 17.8 % compared to 14.5 %, $p = 0.030$). The difference in depth was also not statistically significant between soil classes D1c and D1d. However, the clay content of the Ap-AB horizon of soil class D1c was significantly higher than that of class D1d (17.2 % compared to 15.0 %, $p = 0.030$). These observed differences in texture are in agreement with the decrease in average ECa from class D1a to D1d.

Soil class D2 showed an anthropogenic horizon over coarser sediments in all four ground truth locations. No other horizon type (e.g. Bw, Bg, or 2C) was found in these four profiles. The coarse horizon at the bottom of the four profiles was different from the 2C horizon of the other classes of sub-area D. This was confirmed by differences in the color of the sediments, the shape of the gravels, and the generally higher clay, and water content compared to the 2C horizon of the other soil classes. This soil class was interpreted as the remains of a small brook that was recently buried with anthropogenic filling (also see Appendix A).

3.5 Comparison with patterns in plant stress

In order to verify the ability of the high-resolution soil map to represent agronomically relevant processes, it was compared to patterns in crop stress in sugar beet obtained from satellite imagery (Figure 11). This comparison focused on approximately one fourth of the study area (25.5 ha) covered with sugar beet and considered fields from all four sub-areas. Figure 11 shows the patterns in crop stress determined for field F05 (Figure 11b) and field F07 (Figure 11e). It can be seen that these patterns match well with the high resolution soil map for both fields (Figure 11c and Figure 11f), and the match is visualized in Figure 11d and Figure 11g, where green cells indicate correctly classified cells and red cells indicate incorrectly classified ones.

To quantify the match between the soil map and the patterns in crop stress, the TPR and TNR were first calculated for each class and then aggregated to the field-scale using weighted averaging (Table 7). The TPR represents the percentage of cells that are correctly classified as stressed crops, and ranged from 60.2 to 93.5% for the investigated fields. The weighted average for the study area was 77.9%. The TNR represents the percentage of cells that are correctly classified as healthy crops, and ranged from 62.7 to 97.1% with a weighted average of 89.0% for the study area.

In sub-area A, the TPR is 80.4%, the TNR is 73.6%, and the weighted average is 76.6% (Table 7). The result of the classification in this sub-area is satisfying with a high accuracy in the classification of areas with stressed crops (soil classes A1c-d). In sub-area B, only soil class B1b corresponded to stressed crops and the TPR is 73.1%. All other soil classes corresponded to healthy crops, and the TNR was 95.2%. However, this high TNR is affected by the large area of healthy crops (85%) in this sub-area. Sub-area C is entirely covered with healthy plants. Consequently, it has no TPR and a TNR of 100%. In sub-area D, the TPR is 62.7%, the TNR is 84.6%, and the weighted average is 83.3%. Similar to sub-area B, is mostly covered with healthy crops (~85%, soil classes D1a-c and D2a), resulting in a high TNR. In this sub-area, the relatively poor TPR is most probably connected with the conditions in which field F40 was measured (under heavy rain, the 20th and 21st of October 2016).

Overall, the correspondence between the high-resolution soil map and the satellite image was found to be satisfying, also because the geometry of the areas in which crops are experiencing water stress during drought periods was identified to a reasonable degree.

4. Summary and Conclusions

In this study, multi-configuration EMI measurements were combined with ground truth data to obtain a high-resolution soil map of a 1 x 1 km area. Due to the size of the investigated area and the heterogeneous land management, it was necessary to acquire EMI measurements field by field over a period of several months. Therefore, changes in ECa between fields due to different water content and land management (crop type, fertilization, etc.) were present in the final ECa maps of the study area. To enable a classification of the ECa measurements into areas with similar soil properties, an approach commonly used for the interpretation of multi-band remote sensing data was adopted. For this, a multi-band image was created from the ECa data and a supervised image classification strategy that additionally relied on available low-resolution soil maps was used to divide the study area in a finite number of soil classes. In particular, the study area was first divided in four sub-areas based on the nine available ECa maps and the available soil maps. In a second step, these four sub-areas were further divided in a total of 18 soil classes using a field-by-field analysis. It is clear that the results of such supervised classification depend to some extent on the interpreter, as is the case for many soil maps. Nevertheless, it was found that this approach was most suited to obtain soil information from the EMI measurements in the presence of additional variation due to variable water content and pore water conductivity. Future research could explore the benefit of advanced unsupervised classification methodologies to obtain a more objective approach.

In a next step, we selected 100 locations where soil profile descriptions to a maximum depth of two meters were obtained and a total of 552 samples were collected and analyzed to obtain textural characteristics. The profiles of each class were averaged to obtain typical soil profiles for each soil class with information on horizon type, layer depth, water content, and soil texture. In each sub-area, classes were ordered according to their average ECa. Then, neighboring classes were compared using two tailed *t*-tests that were performed between matching horizons. It was found that there were significant differences between the soil profiles in terms of layering and texture, and that the observed differences were in agreement with the variation of average ECa between different classes. The final product of this study is a 1 m resolution soil map with 18 units with typical soil profile and texture information.

Finally, the high-resolution soil map was compared with patterns in crop stress obtained from a satellite image to verify that the soil map is able to represent such patterns. This evaluation was performed for approximately one fourth of the study area, and it was found that areas with stressed crops matched well with particular soil types. This indicates that the high-resolution soil map obtained from a combination of multi-configuration EMI measurements and ground truth data is useful for defining zones that require variable management within precision agriculture applications. In addition, the high-resolution soil map is useful as input for agro-ecological model applications to predict crop stress as a function of environmental boundary conditions (soil, water availability, crop type). This will be explored in a follow up study.

Acknowledgments

This study was supported by the Deutsche Forschungsgemeinschaft through the Transregional Collaborative Research Center 32 – Patterns in Soil-Vegetation-Atmosphere Systems: Monitoring, Modeling and Data Assimilation. In addition, support was received through the "Terrestrial ENvironmental Observatories" (TERENO), and Advanced Remote Sensing—Ground-Truth Demo and Test Facilities (ACROSS) initiative. We thank Marius Schmidt for his precious help in managing the contacts with the land owners, and Elizabeth Verweij, Igor dal Bo, Zhen Zou, Tao Liu, Philipp Pohlig, Maximillian Kanig, Luka Kurnjek, Xihe Tan, Hui Wang, Michael Lesch, Liza de Quadros, Prakash Satenahalli, and Magdalena Landl for their help during the measurement campaign.

Appendix A – Geomorphological interpretation of EMI data

In this appendix, an interpretation of the geomorphological features that are visible in sub-areas B, C, and D is provided. A comparison between ECa maps and other available data such as morphometric data, historical maps, and historical aerial pictures was essential for the identification of these features and informed the interpretation that was necessary to conduct a proper supervised classification.

To obtain geomorphic information, we used a digital elevation model (DEM) with spatial a resolution of 1 m (Scilands-GmBH, 2013). Additionally, anthropogenic features were considered in the overall interpretation since the area has been cultivated in the last centuries. Finally, the study area was a battlefield in WWII because the Rur river between Düren and Jülich represented a strategic defense line during the invasion of Germany by the Allied forces from December 1944 to February 1945. This resulted in massive bombing runs on the city of Düren and the nearby defensive structures. Aerial pictures and historical maps were georeferenced and used to identify whether observed subsurface structures are associated with war activity.

In sub-area B, the EMI data consistently showed small areas of 1-2 ha with lower ECa compared to the surroundings. The shape of these areas depends on the DOI (see Figure A1a-c for DOIs of 75, 146 and 270 cm respectively) indicating that the presence of shallow structures was associated with the slope that characterizes sub-area B. The shape and the position of different structures along the slope allow a distinction between two regions with different genesis. The first structure (Type 1 in Figure A1a-c) was interpreted as a deposition of coarse material eroded from sub-area A when the channel system was not yet buried under aeolian sediments that led to the formation of small fluvial fans. To support this interpretation, it was found that these features were adjacent to a paleochannel structure of sub-area A intersecting the boundary with sub-area B, and that the ECa pattern showed an elongated shape with low persistence with depth in their distal or proximal portions. The second structure (Type 2 in Figure A1a-c) was interpreted as a feature resulting from both natural and anthropogenic processes. First, shallow and slow movement has moved material from sub-area A to B. However, the observed feature is also related to recent anthropogenic soil management. It is known that the topography of the study area has been reshaped to facilitate agriculture with mechanized equipment (plowing, sowing and harvesting). In addition, the area of the lower Ruhr has been inhabited and farmed for about the last 7000 yrs. Thus, soil erosion since the beginning of arable farming has also contributed to relief flattening.

Several other interesting features can be observed in the ECa values of sub-area C (Figure A**2**). The shape of these structures is characterized by straight lines and approximately square polygons. These structures were characterized by lower ECa values compared to the surroundings and were interpreted as recent anthropogenic activity because of their distinct geometry. To identify the origin of these shapes, we compared the ECa map in Figure A**2**a with georeferenced aerial pictures and historical maps shown in Figure A**2**b and Figure A**2**c, respectively. From the aerial photo taken in November 1944 (USAAF, 1944), it can be concluded that these features were not related to defensive trench systems from WWII (Figure A**2**b). Instead, historical maps suggest that these structures were associated with field boundaries, irrigation channels, and water ponds and reservoirs that were active at the end of the 19th century or before (Figure A**2**c). Similar geometries are also visible in older maps like the *Tranchot* map from Napoleon times dating back to between 1801 and 1809 (map not shown). The ECa and historical maps do not perfectly match, but this could be expected given the limited precision of the older maps and the transient nature of such local water management structures.

More indications for recent anthropogenic activity have been identified in field F39 of sub-area D (Figure A3). This area was characterized by various buried paleochannels, but it is also possible to identify one channel with a strong EMI response (Figure A3a). When comparing the EMI measurements with aerial photos from 1944 (USAAF, 1944) (Figure A3b), we identified a depression that probably corresponds to the remains of a small brook. The channel has been buried with anthropogenic sediments since 1944. The channel geometry matched with the higher ECa values obtained with EMI, and it was still apparent in the DEM where a topographic depression indicated the old position of the channel (compare Figure A3a, Figure A3b and Figure A3c).

References

Ball, G., Hall, D., 1965. A novel method of data analysis and pattern classification. Tch. Report 5RI, Project 5533. Stanford RI, Menlo Park, Ca. USA.

Campbell, R., Bower, C., Richards, L., 1949. Change of electrical conductivity with temperature and the relation of osmotic pressure to electrical conductivity and ion concentration for soil extracts. Soil Science Society of America Journal 13(C), 66-69.

Castrignano, A., Wong, M., Stelluti, M., De Benedetto, D., Sollitto, D., 2012. Use of EMI, gamma-ray emission and GPS height as multi-sensor data for soil characterisation. Geoderma 175, 78-89.

Ciampalini, A., André, F., Garfagnoli, F., Grandjean, G., Lambot, S., Chiarantini, L., Moretti, S., 2015. Improved estimation of soil clay content by the fusion of remote hyperspectral and proximal geophysical sensing. Journal of Applied Geophysics 116, 135-145.

Cockx, L., Van Meirvenne, M., De Vos, B., 2007. Using the EM38DD soil sensor to delineate clay lenses in a sandy forest soil.

Corwin, D., Lesch, S., 2003. Application of soil electrical conductivity to precision agriculture. Agronomy Journal 95(3), 455-471.

Corwin, D., Lesch, S., 2005. Apparent soil electrical conductivity measurements in agriculture. Computers and electronics in agriculture 46(1), 11-43.

De Benedetto, D., Castrignanò, A., Rinaldi, M., Ruggieri, S., Santoro, F., Figorito, B., Gualano, S., Diacono, M., Tamborrino, R., 2013. An approach for delineating homogeneous zones by using multi-sensor data. Geoderma 199, 117-127.

Ding, J., Yu, D., 2014. Monitoring and evaluating spatial variability of soil salinity in dry and wet seasons in the Werigan–Kuqa Oasis, China, using remote sensing and electromagnetic induction instruments. Geoderma 235, 316-322.

ESRI, 2014. ArcGIS Desktop Help.

ESRI, 2016. Esri, DIgitalGlobe, GeoEye, Earthstar Geographics, CNES/Airbus DS, USDA, AEX, Getmapping, Aerogrid, IGN, IGP, swisstopo, and the GIS User Comunity.

ESRI, 2017. ArcGIS Desktop: Release 10.3 Redlands, CA.

European Committee for Standardization, M.C.A.M., B-10000 Brussels, CWA 16373:2011, 2011. Best practice approach for electromagnetic induction (EMI) measurements of the near surface.

Franzen, D.W., Hopkins, D.H., Sweeney, M.D., Ulmer, M.K., Halvorson, A.D., 2002. Evaluation of soil survey scale for zone development of site-specific nitrogen management. Agronomy Journal 94(2), 381-389.

Frederiksen, R.R., Christiansen, A.V., Christensen, S., Rasmussen, K.R., 2017. A direct comparison of EMI data and borehole data on a 1000ha data set. Geoderma 303, 188-195.

Galambošová, J., Rataj, V., Prokeinová, R., Presinska, J., 2014. Determining the management zones with hierarchic and non-hierarchic clustering methods. Research in Agricultural Engineering 60(Special Issue).

GF_Instruments, 2011. CMD electromagnetic conductivity meter user manual V. 1.5 GF Instruments s.r.o. Geophysical Equipment and Services.

Huang, J., Kilminster, T., Barrett-Lennard, E., Triantafilis, J., 2017a. Characterization of field-scale dryland salinity with depth by quasi-3d inversion of DUALEM-1 data. Soil Use and Management 33(2), 205-215.

Huang, J., Lark, R., Robinson, D., Lebron, I., Keith, A., Rawlins, B., Tye, A., Kuras, O., Raines, M., Triantafilis, J., 2014. Scope to predict soil properties at within-field scale from small samples using proximally sensed γ-ray spectrometer and EM induction data. Geoderma 232, 69-80.

Huang, J., McBratney, A., Minasny, B., Triantafilis, J., 2017b. Monitoring and modelling soil water dynamics using electromagnetic conductivity imaging and the ensemble Kalman filter. Geoderma 285, 76-93.

Huang, J., Pedrera-Parrilla, A., Vanderlinden, K., Taguas, E., Gómez, J., Triantafilis, J., 2017c. Potential to map depth-specific soil organic matter content across an olive grove using quasi-2d and quasi-3d inversion of DUALEM-21 data. Catena 152, 207-217.

Jing, Y., Huang, J., Banks, R., Triantafilis, J., 2017. Scope to map soil management units at the district level from remotely sensed γ-ray spectrometry and proximal sensed EM induction data. Soil Use and Management 33(4), 538-552.

Keller, G., Frischknecht, F., 1966. Electrical methods in geophysical prospecting.

Kelley, J., Higgins, C.W., Pahlow, M., Noller, J., 2017. Mapping Soil Texture by Electromagnetic Induction: A Case for Regional Data Coordination. Soil Science Society of America Journal 81(4), 923-931.

King, J., Dampney, P., Lark, R., Wheeler, H., Bradley, R., Mayr, T., 2005. Mapping potential crop management zones within fields: use of yield-map series and patterns of soil physical properties identified by electromagnetic induction sensing. Precision Agriculture 6(2), 167-181.

Klostermann, J., 1992. Das Quartär der Niederrheinischen Bucht: Ablagerungen der letzten Eiszeit am Niederrhein. Geologisches Landesamt Nordrhein-Westfalen.

Lavoué, F., Van Der Kruk, J., Rings, J., André, F., Moghadas, D., Huisman, J., Lambot, S., Weihermüller, L., Vanderborght, J., Vereecken, H., 2010. Electromagnetic induction calibration using apparent electrical conductivity modelling based on electrical resistivity tomography. Near Surface Geophysics 8(6), 553-561.

Machado, F.C., Montanari, R., Shiratsuchi, L.S., Lovera, L.H., Lima, E.d.S., 2015. Spatial dependence of electrical conductivity and chemical properties of the soil by electromagnetic induction. Revista Brasileira de Ciência do Solo 39(4), 1112-1120.

McNeill, J., 1980. Electromagnetic terrain conductivity measurement at low induction numbers. Geonics Limited Ontario, Canada.

Mertens, F., Pätzold, S., Welp, G., 2008. Spatial heterogeneity of soil properties and its mapping with apparent electrical conductivity. Journal of Plant Nutrition and Soil Science 171(2), 146-154.

Mester, A., van der Kruk, J., Zimmermann, E., Vereecken, H., 2011. Quantitative two-layer conductivity inversion of multi-configuration electromagnetic induction measurements. Vadose Zone Journal 10(4), 1319-1330.

Minsley, B., Smith, B., Hammack, R., Sams, J., Veloski, G., 2012. Calibration and filtering strategies for frequency domain electromagnetic data. Journal of Applied Geophysics 80, 56-66.

Nawar, S., Corstanje, R., Halcro, G., Mulla, D., Mouazen, A.M., 2017. Delineation of Soil Management Zones for Variable-Rate Fertilization: A Review, Advances in Agronomy. Elsevier, pp. 175-245.

NRW, 1960. Soil Taxation Map. 1960.Bödenschätrzungskarte: Bearbeitet nach den amtlichen Unterlagen der Bodenschätzung und des Geologichen Landesamts Nordrhein-Westfalen vom Regierungspräsident in Aachen und dem Geologischen Ladesamt Nordrhein-Westfalen 1960. Landesvermessungsamt Nordrhein-Westfalen.

NRW, 2017. Bezirksregierung Köln - The WebAtlasDE is an Internet computer service developed jointly by the federal (North Rhine-Westfphalia) and state governments and provided by the Federal Agency for Cartography and Geodesy.

Oldoni, H., Bassoi, L.H., 2016. Delineation of irrigation management zones in a Quartzipsamment of the Brazilian semiarid region. Pesquisa Agropecuária Brasileira 51(9), 1283-1294.

Patzold, S., Mertens, F., Bornemann, L., Koleczek, B., Franke, J., Feilhauer, H., Welp, G., 2008. Soil heterogeneity at the field scale: a challenge for precision crop protection. Precision Agriculture 9(6), 367-390.

Richards, J., 1999. Remote sensing digital image analysis, 3. Springer.

Robinet, J., von Hebel, C., Govers, G., van der Kruk, J., Minella, J.P., Schlesner, A., Ameijeiras-Mariño, Y., Vanderborght, J., 2018. Spatial variability of soil water content and soil electrical conductivity across scales derived from Electromagnetic Induction and Time Domain Reflectometry. Geoderma 314, 160-174.

Robinson, D., Abdu, H., Lebron, I., Jones, S., 2012. Imaging of hill-slope soil moisture wetting patterns in a semi-arid oak savanna catchment using time-lapse electromagnetic induction. Journal of Hydrology 416, 39-49.

Robinson, D., Binley, A., Crook, N., Day-Lewis, F., Ferré, T., Grauch, V., Knight, R., Knoll, M., Lakshmi, V., Miller, R., 2008. Advancing process-based watershed hydrological research using near-surface geophysics: A vision for, and review of, electrical and magnetic geophysical methods. Hydrological Processes 22(18), 3604-3635.

Röhrig, W., 1996. Bodenkarte 1:5000 zur landwirtschaftlichen Standorterkundung (BK5ÖL). Geologischen Landesamt Nordrhein-Westfalien.

Rosgen, D., 1994. A classification of natural rivers. Catena 22(3), 169-199.

Rudolph, S., Marchant, B.P., Weihermüller, L., Vereecken, H., 2018. Assessment of the position accuracy of a single-frequency GPS receiver designed for electromagnetic induction surveys. Precision Agriculture, 1-21.

Rudolph, S., van der Kruk, J., Von Hebel, C., Ali, M., Herbst, M., Montzka, C., Pätzold, S., Robinson, D., Vereecken, H., Weihermüller, L., 2015. Linking satellite derived LAI patterns with subsoil heterogeneity using large-scale ground-based electromagnetic induction measurements. Geoderma 241, 262-271.

Scilands-GmBH, 2013. Digital Elevation Model 1m mosaic data (Section 4), based on data from Bezirksregierung Köln, Göttingen, Rermany. CRC/TR32 Database (TR32DB). Accessed from http://www.tr32db.uni-koeln.de/data.php?dataID=440 at 2017-07-11.

Shanahan, P., Binley, A., Whalley, W., Watts, C., 2015. The use of electromagnetic induction to monitor changes in soil moisture profiles beneath different wheat genotypes. Soil Science Society of America Journal 79(2), 459-466.

Sheets, K., Hendrickx, J., 1995. Noninvasive soil water content measurement using electromagnetic induction. Water resources research 31(10), 2401-2409.

Simmer, C., Thiele-Eich, I., Masbou, M., Amelung, W., Bogena, H., Crewell, S., Diekkrüger, B., Ewert, F., Hendricks Franssen, H.-J., Huisman, J.A., 2015. Monitoring and modeling the terrestrial system from pores to catchments: the transregional collaborative research center on patterns in the soil–vegetation–atmosphere system. Bulletin of the American Meteorological Society 96(10), 1765-1787.

Sponagel, H., Grottenthaler, K.J., Hartmann, R., Hartwich, P., Janetzko, P., Joisten, H., Kühn, D., Sabel, K.J., Tradl, R., 2005. Bodenkundliche Kartieranleitung (German Manual of Soil Mapping, KA5) (fifth ed.), Bundesanstalt für Geowissenschaften und Rohstoffe, Hannover (2005). Schweizerbart.

Stadler, A., Rudolph, S., Kupisch, M., Langensiepen, M., van der Kruk, J., Ewert, F., 2015. Quantifying the effects of soil variability on crop growth using apparent soil electrical conductivity measurements. European journal of agronomy 64, 8-20.

Tan, X., Mester, A., von Hebel, C., Zimermann, E., Vereecken, H., van Waasen, S., van der Kruk, J., 2018. Simultaneous calibration and inversion algorithm for multi-configuration electromagnetic induction data acquired at multiple elevations. Submiotted to Gephysics

Taylor, J.C., Wood, G., Earl, R., Godwin, R., 2003. Soil factors and their influence on within-field crop variability, part II: spatial analysis and determination of management zones. Biosystems engineering 84(4), 441-453.

Thiesson, J., Kessouri, P., Schamper, C., Tabbagh, A., 2014. Calibration of frequency-domain electromagnetic devices used in near-surface surveying. Near Surface Geophysics 12(4), 481-491.

Triantafilis, J., Kerridge, B., Buchanan, S.M., 2009. Digital soil-class mapping from proximal and remotely sensed data at the field level. Agronomy Journal 101(4), 841-853.

Uribeetxebarria, A., Arnó, J., Martínez-Casasnovas, J.A., 2018. Apparent electrical conductivity and multivariate analysis of soil properties to assess soil constraints in orchards affected by previous parcelling. Geoderma 319, 185-193.

USAAF, 1944. Picture ID: 2016, Mission ID: 33-0778. Luftbilddatenbank, Dr Carls GMBH.

van Dam, R., 2012. Landform characterization using geophysics—Recent advances, applications, and emerging tools. Geomorphology 137(1), 57-73.

Vandenberghe, J., Van Overmeeren, R., 1999. Ground penetrating radar images of selected fluvial deposits in the Netherlands. Sedimentary Geology 128(3), 245-270.

von Hebel, C., Rudolph, S., Mester, A., Huisman, J., Kumbhar, P., Vereecken, H., van der Kruk, J., 2014. Three-dimensional imaging of subsurface structural patterns using quantitative large-scale multiconfiguration electromagnetic induction data. Water Resources Research 50(3), 2732-2748.

Vos, C., Don, A., Prietz, R., Heidkamp, A., Freibauer, A., 2016. Field-based soil-texture estimates could replace laboratory analysis. Geoderma 267, 215-219.

Ward, S., Hohmann, G., 1988. Electromagnetic theory for geophysical applications. Electromagnetic methods in applied geophysics 1(3), 131-311.

WRB, I.W.G., 2015. World Reference Base for Soil Resources 2014, update 2015. International soil classification system for naming soils and creating legends for soil maps. World Soil Resources Reports No. 106. FAO, Rome.

Yao, R., Yang, J., Wu, D., Xie, W., Gao, P., Jin, W., 2016. Digital mapping of soil salinity and crop yield across a coastal agricultural landscape using repeated electromagnetic induction (EMI) surveys. PloS one 11(5), e0153377.

Zare, E., Huang, J., Triantafilis, J., 2016. Identifying soil landscape units at the district scale by numerically clustering remote and proximal sensed data. Computers and Electronics in Agriculture 127, 510-520.

Tables

Table 1 – EMI instrument configurations, coil separations, depth of investigation (DOI) and frequency for the CMD Mini Explorer and the CMD Mini Explorer - Special Edition.

EMI instrument	Receivers	Orientation	Separation [cm]	DOI [cm]	Frequency [kHz]
Mini Explorer	3	VCP	32	0-24	30
		VCP	71	0-53	
		VCP	118	0-89	
Mini Explorer Special Edition	6	HCP	35	0-52	25.17
		HCP	50	0-75	
		HCP	71	0-107	
		HCP	97	0-146	
		HCP	135	0-203	
		HCP	180	0-270	

Table 2 - Average (avg.), and standard deviation (σ) of measured ECa values (mS/m) obtained with different coil configurations and separations for sub-areas A to D.

	Sub-Area D		**Sub-Area C**		**Sub-Area B**		**Sub-Area A**	
Configuration	Avg.	σ	Avg.	σ	Avg.	σ	Avg.	σ
VCP 32cm	13.6	5.3	16.1	5.8	10.5	6.0	8.7	4.0
VCP 71cm	17.5	4.3	22.0	4.8	15.1	4.0	10.6	3.2
VCP 118cm	18.8	4.0	24.5	4.6	16.6	3.3	11.4	3.1
HCP 35cm	15.6	3.9	18.8	4.2	14.0	2.1	10.7	2.8
HCP 50cm	16.5	3.3	20.6	4.0	14.7	2.2	11.1	2.6

HCP 71cm	16.5	3.0	21.2	3.7	15.0	2.1	10.9	2.2
HCP 97cm	16.2	2.9	21.6	3.1	15.7	1.8	12.2	1.8
HCP 135cm	16.8	3.1	23.1	3.4	17.1	2.1	12.2	1.9
HCP 180cm	17.9	3.2	25.3	3.7	19.4	2.2	13.0	1.9

Table 3 – Average (Avg.) and Standard deviation ($\boldsymbol{\sigma}$) of the measured ECa values (mS/m) obtained with the six HCP coil configurations in the four classes of sub-area A.

	A1a		**A1b**		**A1c**		**A1d**	
Config.	**Avg.**	**σ**	**Avg.**	**σ**	**Avg.**	**σ**	**Avg.**	**σ**
HCP 035	12.5	2.9	10.8	2.3	9.6	2.3	8.3	1.9
HCP 050	12.9	2.5	11.1	2.1	10.0	1.9	8.6	1.5
HCP 071	12.5	2.2	10.9	1.6	10.0	1.6	8.8	1.3
HCP 097	12.7	1.8	11.1	1.3	10.3	1.3	9.4	1.1
HCP 130	12.7	1.8	11.1	1.4	10.3	1.3	9.9	1.2
HCP 180	13.6	1.9	11.8	1.3	11.1	1.3	10.8	1.2

Table 4 - Average (Avg.) and Standard deviation ($\boldsymbol{\sigma}$) of the measured ECa values (mS/m) obtained with the six HCP coil configurations in the four classes of sub-area B.

	B1a		**B1b**		**B2a**		**B2b**		**B2c**	
Config.	**Mean**	**σ**	**Mean**	**σ**	**Mean**	**σ**	**Mean**	**σ**	**Mean**	**σ**
HCP 035	16.1	2.0	13.3	1.6	14.7	2.5	14.3	2.5	12.6	2.0
HCP 050	16.9	2.2	14.2	1.9	15.5	2.4	14.9	2.2	13.2	2.1
HCP 071	17.2	1.9	14.6	1.8	15.8	2.1	15.2	2.1	13.4	1.9
HCP 097	17.7	1.6	15.4	1.0	16.6	1.7	15.8	1.7	14.0	1.5

HCP 130	19.4	1.7	17.0	1.3	18.0	2.1	17.3	2.3	15.1	1.9
HCP 180	21.7	1.9	19.5	1.3	20.2	2.2	19.5	2.4	17.0	2.1

Table 5 - Average (Avg.) and Standard deviation ($\boldsymbol{\sigma}$) of the measured ECa values (mS/m) obtained with the six HCP coil configurations in the four classes of sub-area C.

	C1a		**C1b**		**C2a**		**C2b**	
Config.	**Mean**	**σ**	**Mean**	**σ**	**Mean**	**σ**	**Mean**	**σ**
HCP 035	20.0	4.0	18.3	3.8	19.6	4.9	19.0	4.0
HCP 050	22.1	3.8	20.1	3.4	21.5	3.9	19.9	3.7
HCP 071	22.7	3.6	20.8	3.1	21.6	3.3	19.8	3.4
HCP 097	22.9	2.8	21.3	2.7	21.3	2.7	19.9	3.4
HCP 130	24.5	3.1	22.8	2.8	22.8	2.9	20.7	3.2
HCP 180	26.8	3.3	25.2	3.0	25.1	3.3	22.7	4.0

Table 6 - Average (Avg.) and Standard deviation ($\boldsymbol{\sigma}$) of the measured ECa values (mS/m) obtained with the six HCP coil configurations in the four classes of sub-area D.

	D1a		**D1b**		**D1c**		**D1d**		**D2**	
Config.	**Mean**	**σ**	**Mean**	**σ**	**Mean**	**σ**	**Mean**	**σ**	**Mean**	**σ**
HCP 035	17.4	3.0	15.7	3.6	12.3	2.1	11.1	2.1	21.0	1.9
HCP 050	18.8	2.8	16.4	2.7	13.5	1.5	13.7	1.3	21.6	1.9
HCP 071	19.0	2.7	16.4	2.4	13.7	1.4	12.6	1.3	20.8	1.4
HCP 097	19.0	2.6	16.2	2.4	13.9	1.6	12.7	1.4	20.3	1.8
HCP 130	19.7	2.8	16.6	2.3	14.0	1.2	13.1	1.4	19.8	1.9
HCP 180	20.8	3.0	17.8	2.5	15.1	1.3	14.5	1.5	20.2	1.9

Table 7 – True positive ratios (TPR), true negative ratios (TNR), and total percentage of correctly classified cells (TOT) resulting from the comparison with satellite image.

	TPR (%)	TNR (%)	TOT (%)
F05	87.0	73.6	79.0
F07	76.9	96.4	90.5
F08	93.5	97.1	96.6
F17a	89.6	62.7	70.4
F22b	74.0	77.4	76.2
F23	90.1	95.7	94.5
F24	91.0	96.1	95.2
F39	64.8	92.1	91.0
F40	60.2	89.0	88.1
F49	67.7	75.7	72.5
Sub-area A	80.4	73.6	76.6
Sub-area B	73.1	95.2	92.0
Sub-area C	ND	100.0	100.0
Sub-area D	62.7	84.6	83.3
1 x 1 km	77.9	89.0	87.2

List of Figures

Figure 1. a) Satellite image of the study area (ESRI, 2016) with the measured fields and respective codes, b) 1:5000 soil map of the study area where the locations of the upper terrace (UT) and lower terrace (LT) are shown, c) digitized Soil Taxation Map (NRW, 1960) sheets 510410 and 510411.

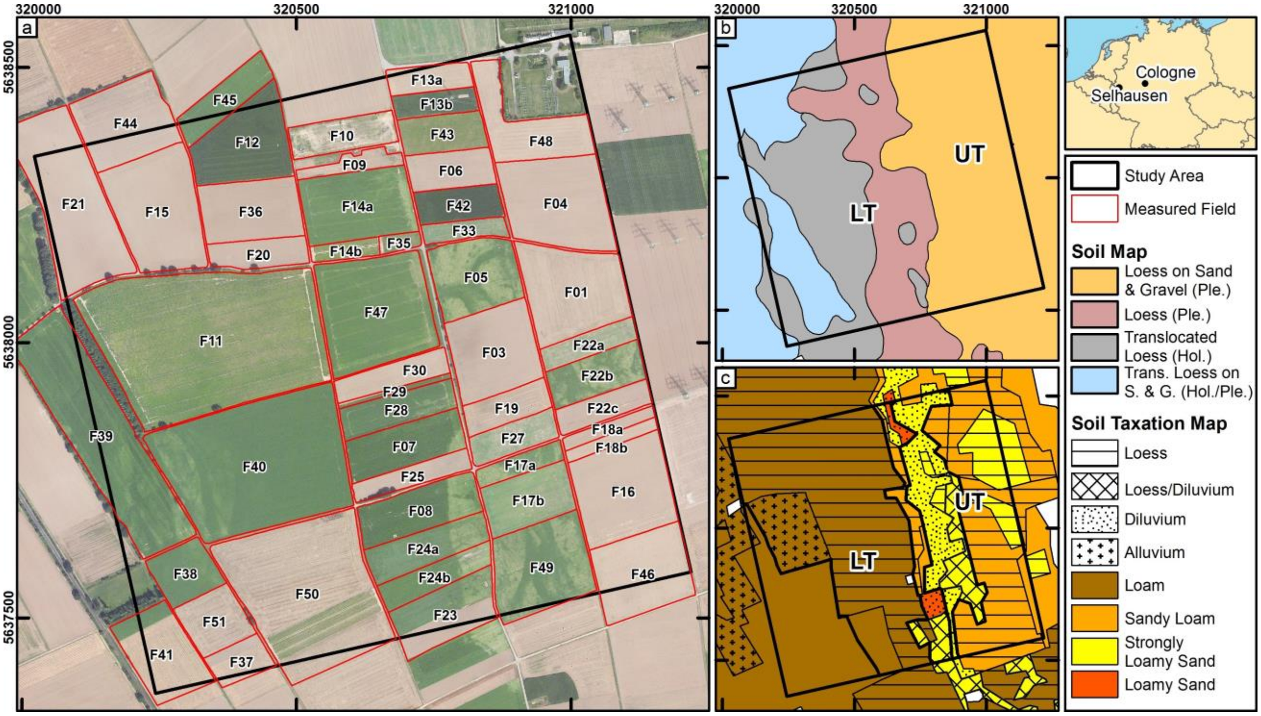

Figure 2. Local sensitivity function for the nine coil separations in the VCP and HCP loop orientation with the separations that are shown in Table 1.

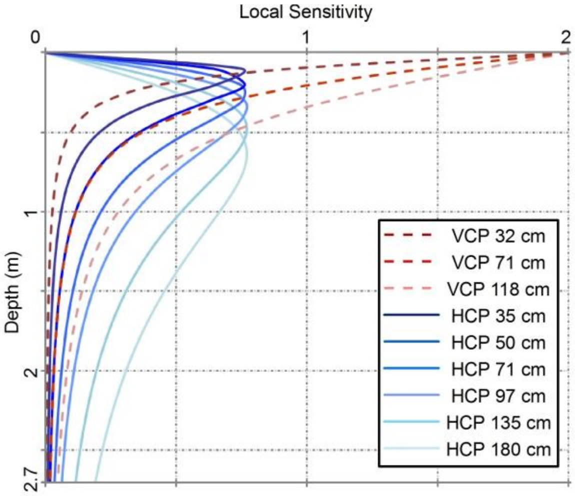

Figure 3. Flowchart of the supervised classification methodology.

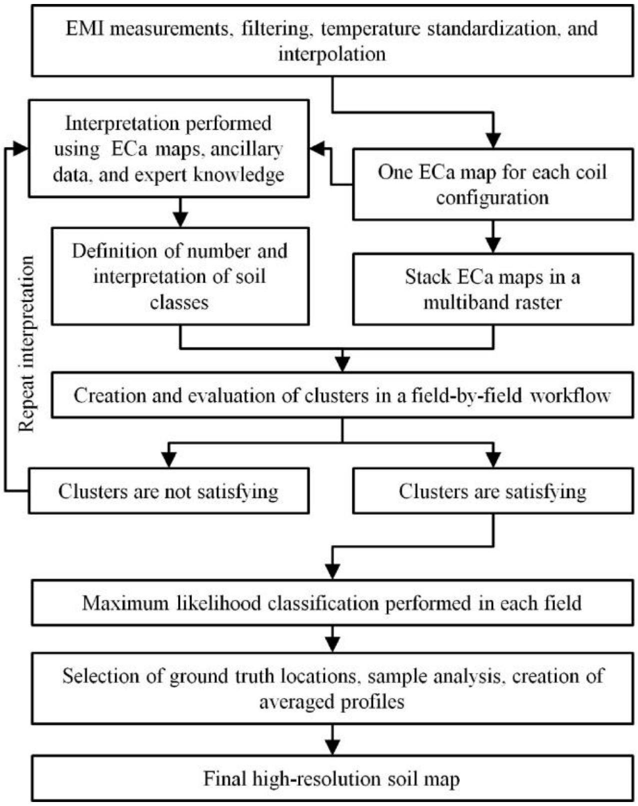

Figure 4. Multiband raster image from the ECa interpolation maps on F05. The 6 bands are the 6 coil distances in HCP configuration of the CMD Mini Explorer – Special Edition.

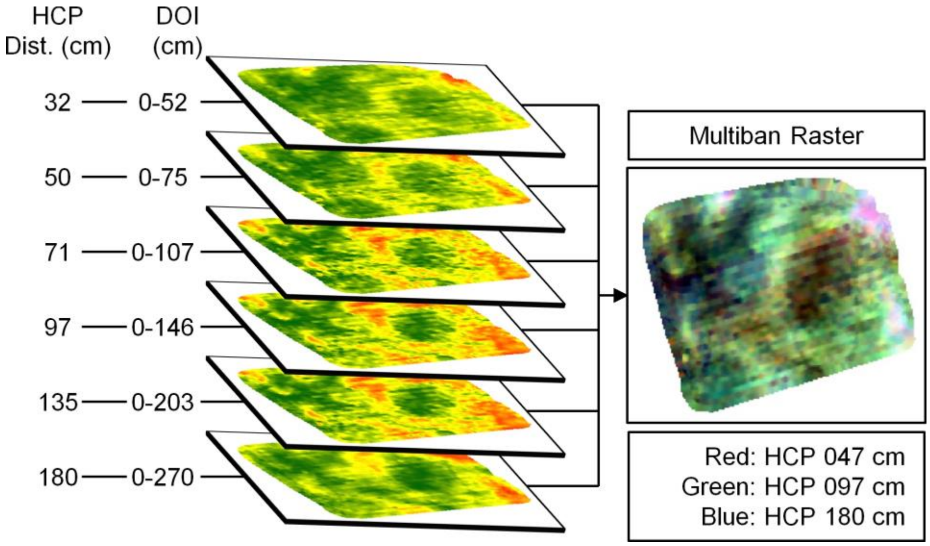

Figure 5. ECa maps of the six HCP configurations: a) HCP 35 cm with lines from the 1:5,000 soil map, b) HCP 50 cm with lines from the soil taxation map, c) HCP 71 cm with subdivision of the study area in four geomorphological sub-areas A, B, C, and D, d) HCP 97 cm with evidence of buried irrigation channels and water ponds (dashed line), e) HCP 118 cm, f) HCP 180 cm.

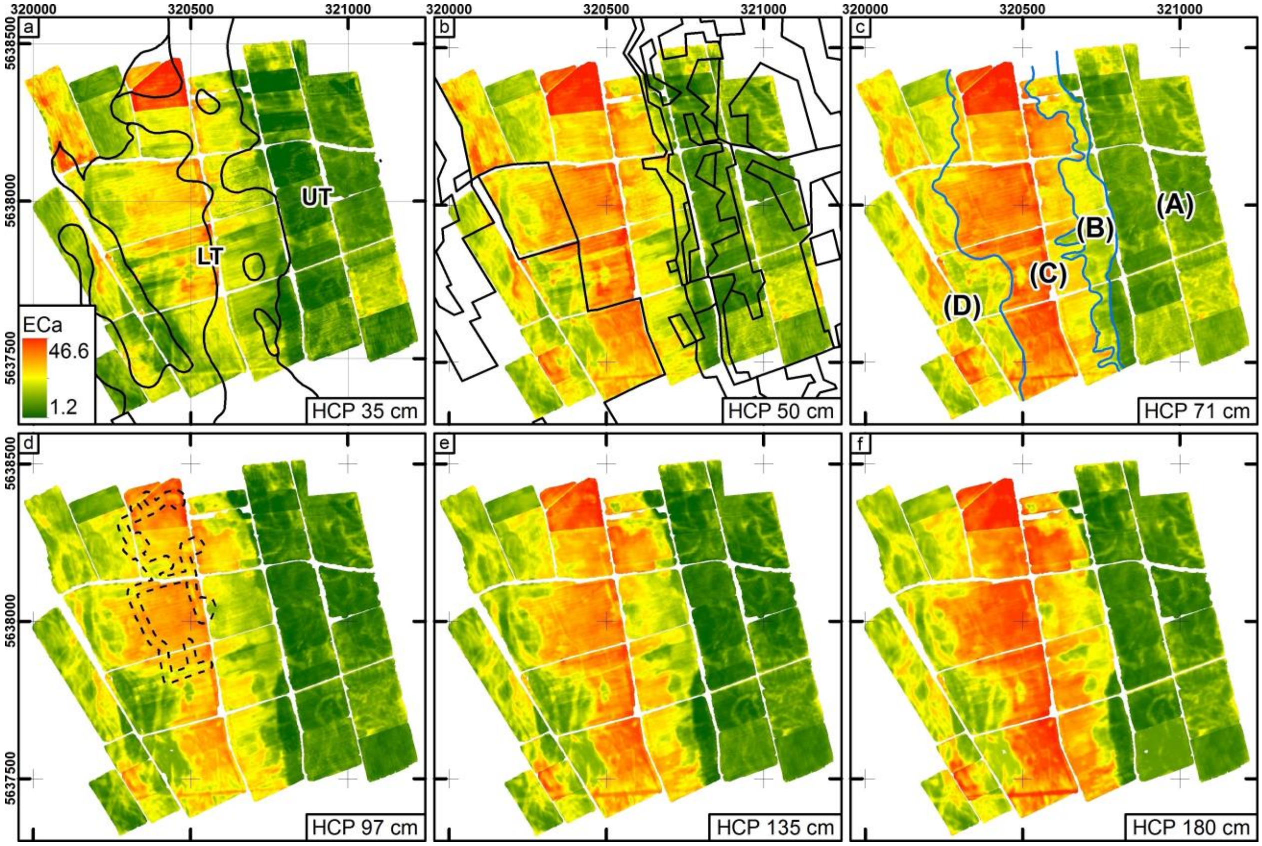

Figure 6. a) Variation in ECa between fields measured within 24h on August the 25th 2016, b) variation in ECa between fields measured at different times (measurement dates given after field abbreviation).

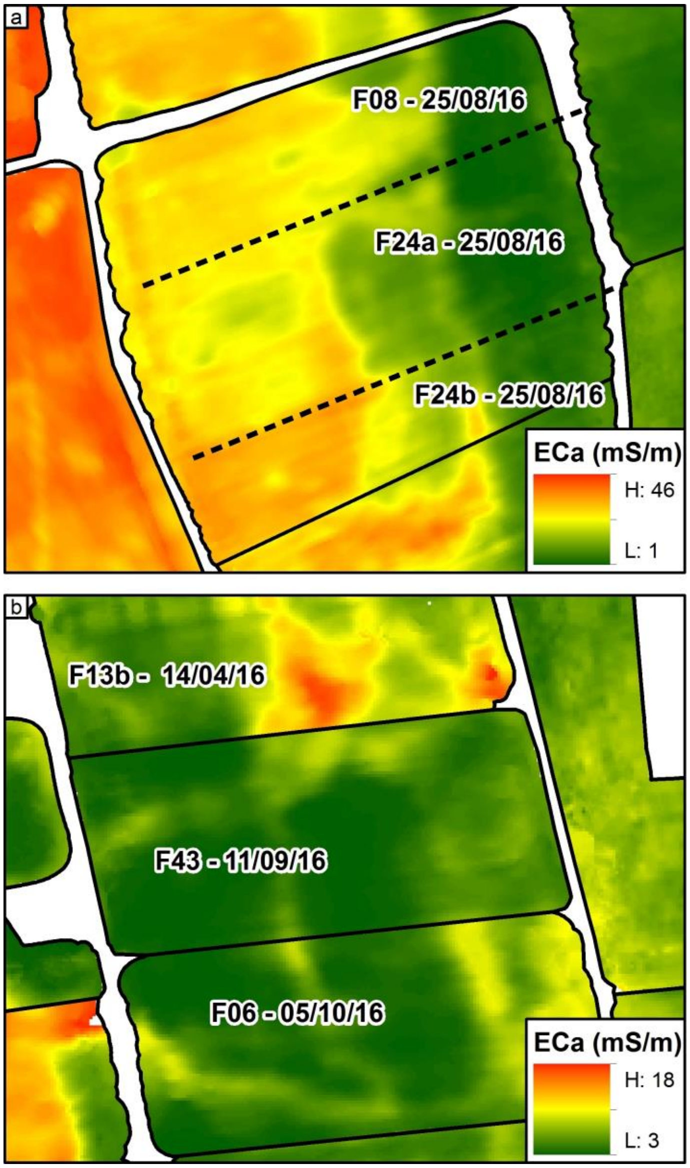

Figure 7. a) ECa map of the HCP 97 cm configuration in sub-area A, b) classified ECa map of sub-area A with the locations of the ground truth points, c) averaged soil profiles for each of the four classes with a description of the statistically significant differences in texture and layers depth between classes A1a-A1b, A1b-A1c, and A1c-A1d. Note that the ECa scale for panel a) differs from the one in Figure 5 to improve visualization.

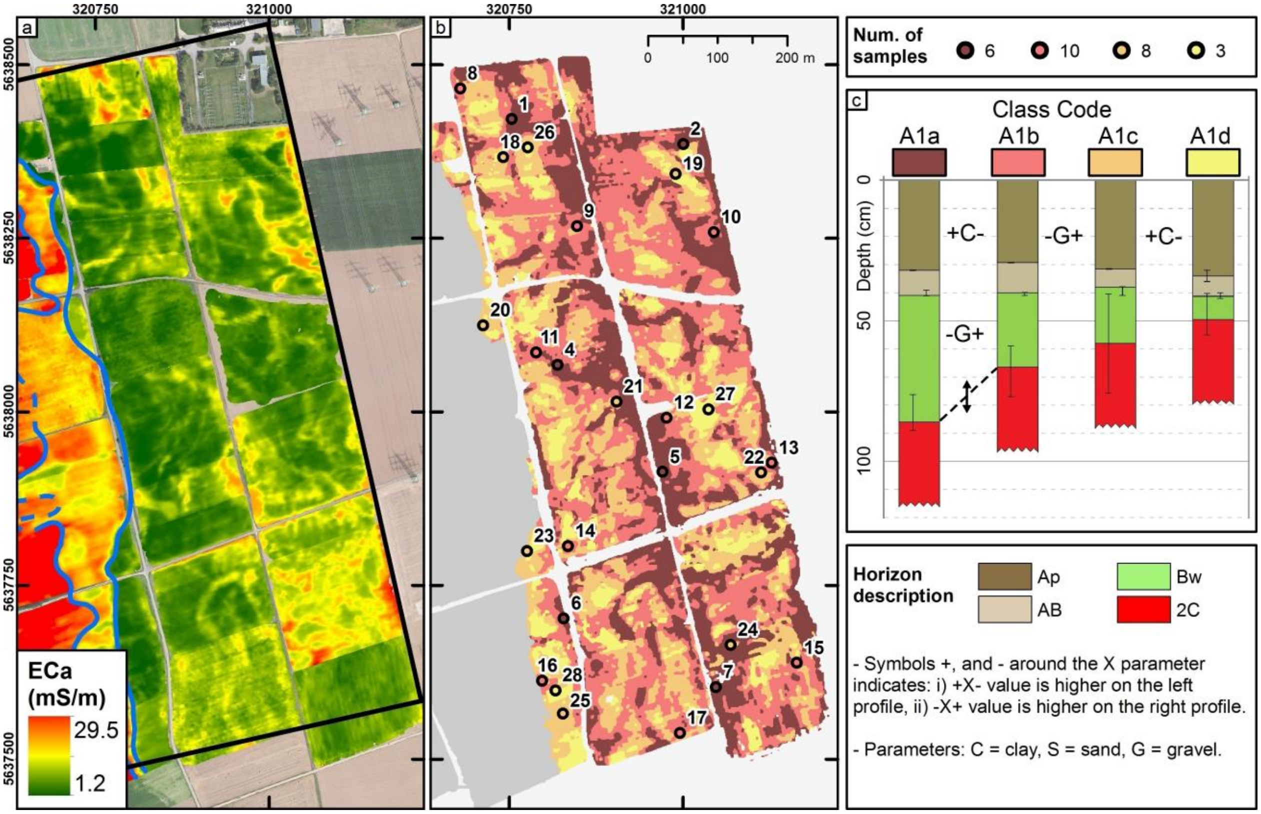

- Symbols +, and - around the X parameter indicates: i) +X- value is higher on the left profile, ii) -X+ value is higher on the right profile.

- Parameters: C = clay, S = sand, G = gravel.

Figure 8. a) ECa map of the HCP 97 cm configuration in sub-area B, b) classified ECa map of sub-area B with the locations of the ground truth points, c-d) averaged soil profiles for each of the four classes with a description of the statistically significant differences in texture between classes B1a-B1b, B2a-B2b, and B2b-B2c.

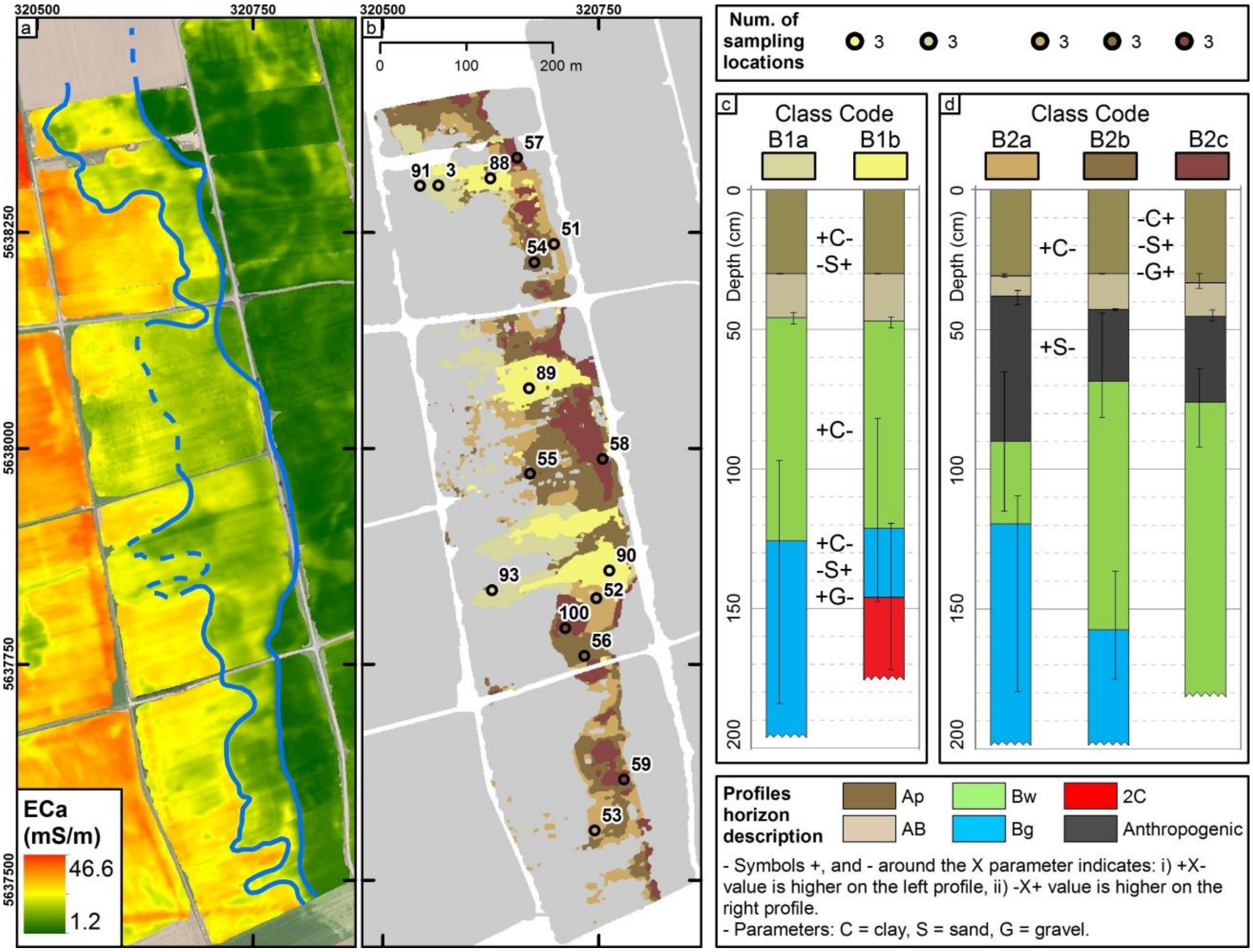

Figure 9. a) ECa map of the HCP 97 cm configuration in sub-area C, b) classified ECa map of sub-area C with the locations of the ground truth points, c-d) averaged soil profiles for each of the four classes with a description of the statistically significant differences in texture and layers depth between classes C1a-C1b and C2a-C2b.

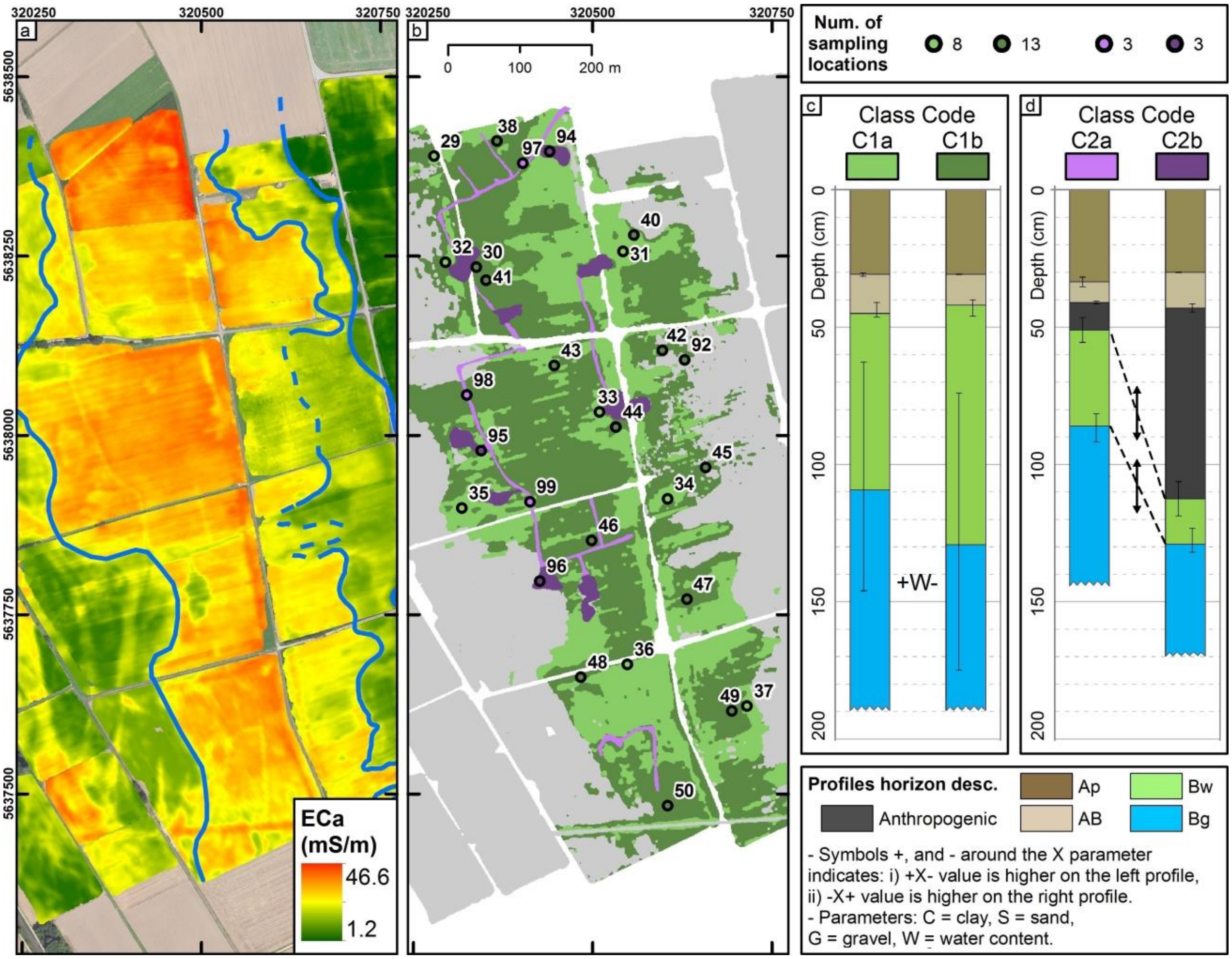

Figure 10. a) ECa map of the HCP 97 cm configuration in sub-area D, b) classified ECa map of sub-area D with the locations of the ground truth points, c) averaged soil profiles for each of the four classes with a description of the statistically significant differences in texture and layers depth between classes D1a-D1b, D1b-D1c, and D1c-D1d.

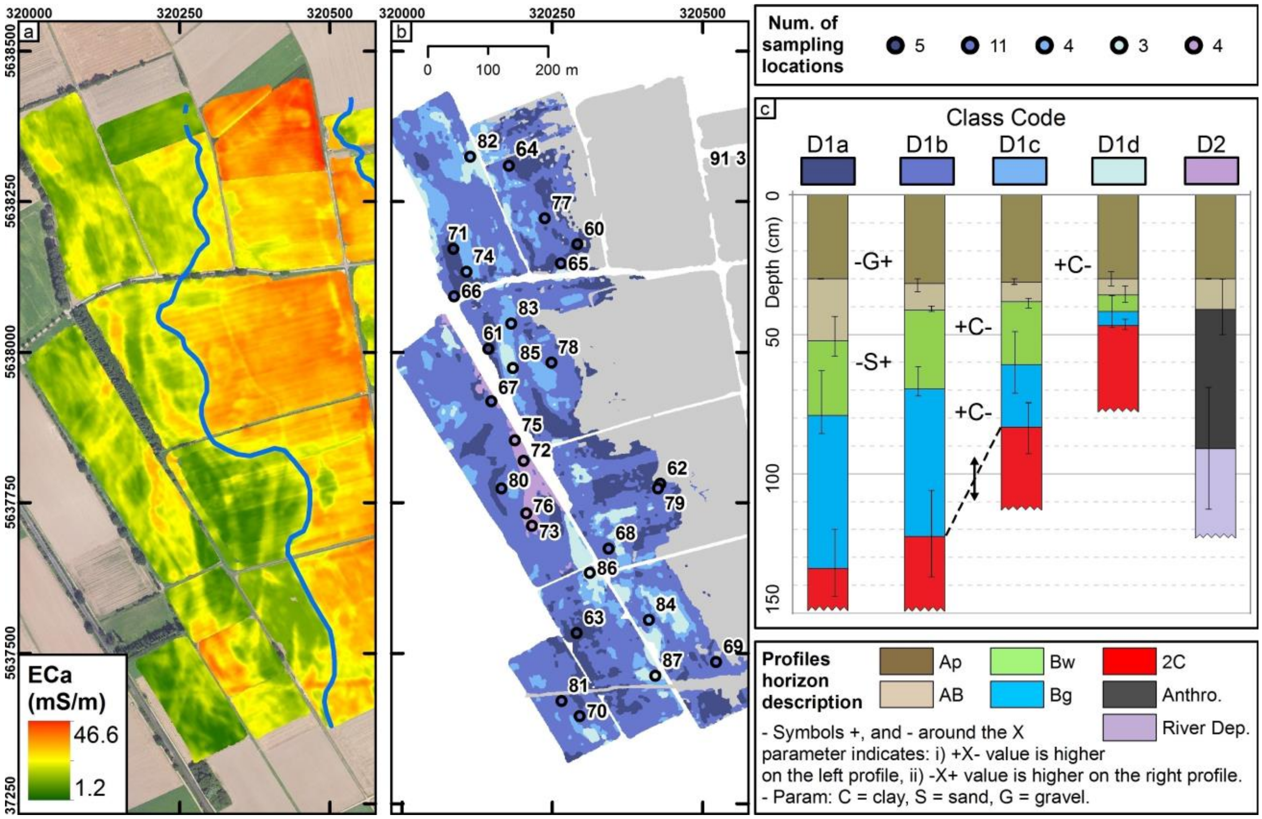

Figure 11. a) Satellite image (ESRI, 2016) of the study area with highlights on the fields cropped with sugar beet, b) digitized patterns in crop stress in F05 (F07 shown in e), c) comparison between classified map and patterns in crop stress on F05 (F07 shown in f), d) correctly classified cells (green) and incorrectly classified one (red) on F05 (F07 shown in g).

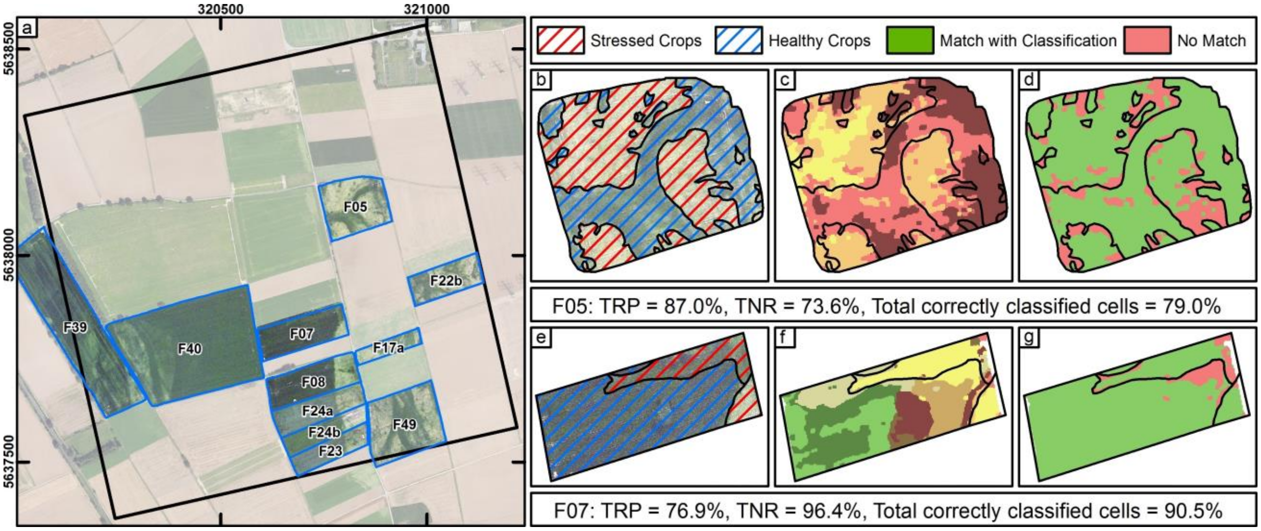

Figure A1. Shallow structures of type 1 and 2 visible along the slope in sub-area B. The interpolated ECa values are shown for a) HCP 49cm, b) HCP 97cm, and c) HCP 180cm.

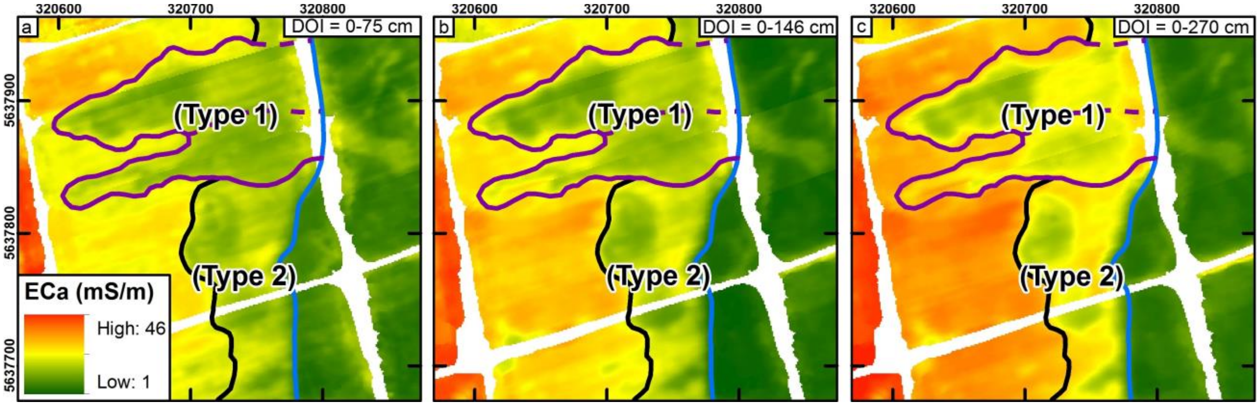

Figure A2. Geometry of anthropogenic features highlighted by a) ECa maps with HCP 97cm configuration compared with b) aerial photo from 19th November 1944 and c) historical map from 1881-1912 (NRW, 2017).

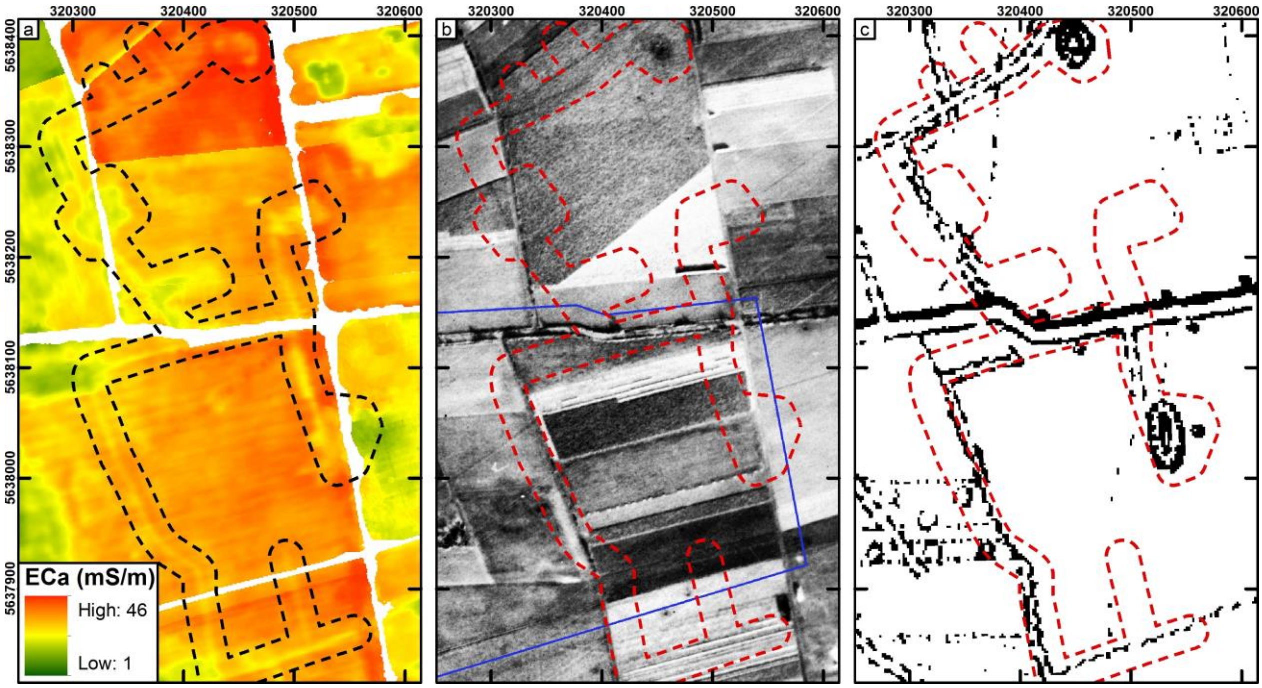

Figure A3. a) ECa maps for HCP 97 cm configuration highlighting a buried structure with a strong EMI response, b) aerial picture from 19th of November 1944 (USAAF, 1944), and c) DEM with 0.5 m spaced contour lines.